Topological defects induce layer formation in *Myxococcus xanthus* colonies

Katherine Copenhagen,[1, *] Ricard Alert,[1, 2, *] Ned S. Wingreen,[1, 3] and Joshua W. Shaevitz[1, 4]

[1]*Lewis-Sigler Institute for Integrative Genomics, Princeton University, Princeton, NJ 08544, USA*
[2]*Princeton Center for Theoretical Science, Princeton University, Princeton, NJ 08544, USA*
[3]*Department of Molecular Biology, Princeton University, Princeton, NJ 08544, USA*
[4]*Joseph Henry Laboratories of Physics, Princeton University, Princeton, NJ 08544, USA*
(Dated: January 22, 2020)

The soil bacterium *Myxococcus xanthus* lives in densely packed groups that form dynamic three-dimensional patterns in response to environmental changes, such as droplet-like fruiting bodies during starvation. The development of these multicellular structures begins with the sequential formation of cell layers in a process that is poorly understood. Using confocal three-dimensional imaging, we find that motile rod-shaped *M. xanthus* cells are densely packed and aligned in each layer, forming an active nematic liquid crystal. Cell alignment is nearly perfect throughout the population except at point defects that carry half-integer topological charge. We observe that new cell layers preferentially form at the position of $+1/2$ defects, whereas holes open at $-1/2$ defects. To explain these findings, we model the bacterial colony as an extensile active nematic fluid with anisotropic friction. In agreement with our experimental measurements, this model predicts an influx of cells toward $+1/2$ defects, and an outflux of cells from $-1/2$ defects. Our results suggest that cell motility and mechanical cell-cell interactions are sufficient to induce the formation of cell layers at topological defects, thereby seeding fruiting bodies in colonies of *M. xanthus*.

The rod-shaped soil bacterium *Myxococcus xanthus* lives in colonies of millions of individual cells that migrate on surfaces. These colonies exhibit a wide range of motility-driven collective behaviors including rippling during predation and fruiting body formation in response to starvation [1–4]. When nutrients are scarce, individual cells alter their motility to drive the population from a thin sheet coating the underlying substrate to a series of dome-shaped multicellular structures called fruiting bodies [5]. The first step in this process is the sequential formation of cell layers on top of an original cell monolayer [6, 7]. However, the physical mechanism underlying layered growth remains largely unknown.

To address how new cell layers emerge from preexisting ones, we imaged the motion of *M. xanthus* cells on an agar substrate using a three-dimensional, laser scanning confocal microscope with subcellular resolution (Methods). This instrument measures light reflected from the surface of the sample and does not require fluorescence or cell labeling. By sampling a stack of positions along the microscope axis, we measured both the height and the reflectance fields (Figs. 1a to 1c). Simultaneous recording of these two complementary fields allows us to examine the relation between cell motility and the formation of cell layers.

We performed experiments in the presence of nutrients. In these conditions, the dimensionless inverse Péclet number that characterizes the persistence of cell migration is $\mathrm{Pe_r^{-1}} = 1.28 \pm 0.09$ (Methods, Fig. S1), too high to form fruiting bodies [5]. Instead, the colony remains as a thin sheet wetting the substrate, with new cell layers and holes continuously appearing and disappearing (Movies S1 and S2). Images of the reflectance field revealed that the rod-shaped *M. xanthus* cells are densely packed, aligned with neighboring cells, and retain their motility (Fig. 1b, Movie S1). The height field showed
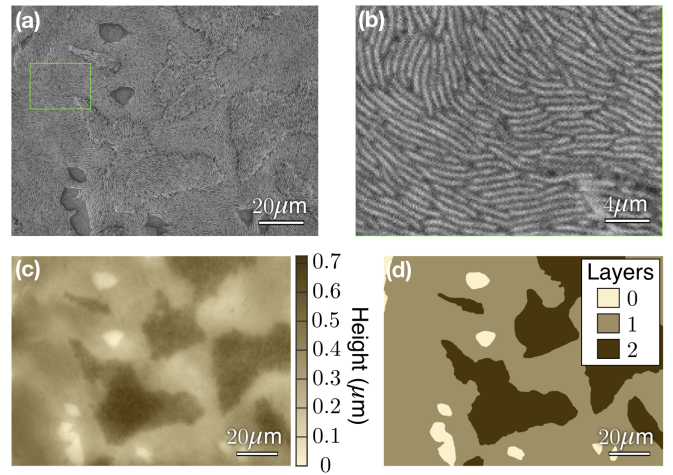

Figure 1: Dense colonies of *M. xanthus* form layered active nematic liquid crystals. Sub-cellular resolution images of the reflectance field (**a**, **b**), height field (**c**), and layer-count field (**d**) of a layered *M. xanthus* colony. 0 layers corresponds to the height of the agar substrate. The zoomed-in view (**b**) of the green box in **a** reveals cell alignment.

that the colony organizes into discrete layers rather than a continuous distribution of heights (Fig. 1c). We thresholded the height data at different levels to measure the number of layers at every position in the image (Fig. 1d, Methods, Fig. S2).

Densely-packed, motile, rod-shaped objects can form a state of matter called an active nematic liquid crystal [8]. Active nematics have rich emergent physics resulting from the interplay between active stresses, here due to cell motility, and orientational order, here due to the cell alignment [8–10]. To quantify orientational order in the *M. xanthus* colony, we used the reflectance field to measure both the degree of alignment $S(\mathbf{r}, t)$ and the cell orientation angle $\theta(\mathbf{r}, t)$ (Figs. 2a and 2b, Methods, Movies S3 and S4). The orientation angle varies

---
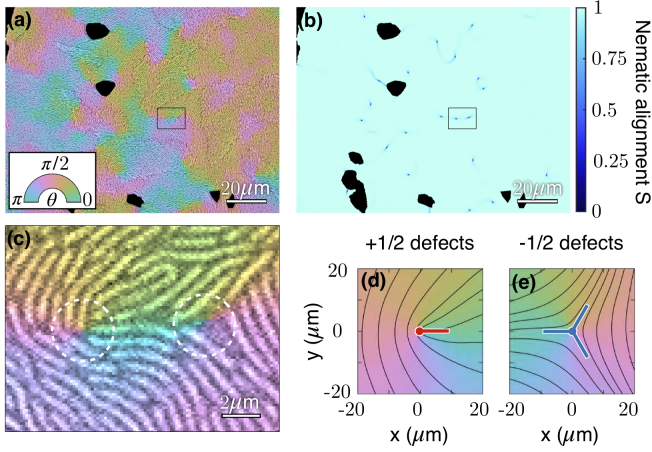* These authors contributed equally to this work.

Figure 2: Nematic alignment and topological defects in *M. xanthus* colonies. (**a**) Nematic cell-orientation angle field $\theta(\mathbf{r})$ overlaid on a reflectance image of a colony. (**b**) Nematic alignment field $S(\mathbf{r})$ for the region shown in **a**. The points at which S approaches 0 are topological defects. (**c**) Zoomed-in view of the black box in **a**; the white dashed lines encircle a $+1/2$ defect (left) and a $-1/2$ defect (right) of the nematic cell alignment. (**d**, **e**) Average angle field measured around $+1/2$ and $-1/2$ defects, respectively. Lines indicate the local axis of cell alignment. $+1/2$ ($-1/2$) defects are labeled with a red (blue) point at the defect core and segments along their axes of symmetry.

smoothly throughout most of the colony, with a correlation length $\ell_{\mathrm{n}} \approx 16.0 \pm 0.5\,\mu$m (Fig. S3). However, at a discrete set of points known as topological defects all orientations meet and hence the orientation angle is singular (Figs. 2a and 2c). At the defect points, alignment is lost ($S = 0$, Fig. 2b). Consistent with the nematic symmetry of cell alignment, we observe defects with half-integer topological charges of $\pm 1/2$ (Figs. 2c to 2e) [11]. Whereas $+1/2$ defects have one axis of symmetry (red segment, Fig. 2d), $-1/2$ defects have three axes of symmetry (blue segments, Fig. 2e). As expected in an active nematic [8, 12, 13], defects are spontaneously created and annihilated either in oppositely-charged pairs or individually at boundaries of a layer (Movie S5).

Similar defect dynamics have been found in other systems including vibrated granular rods [14], mixtures of cytoskeletal filaments and molecular motors [15, 16], monolayers of mesenchymal and epithelial cells [17–20], growing bacterial colonies [21–23], and colonies of swarming filamentous bacteria [24]. In some cell populations, topological defects influence collective cell motion and can even trigger intracellular responses [25]. Both in suspensions of bacteria swimming in passive liquid crystals [26, 27] and in mesenchymal cell monolayers [18], cells were found to accumulate around $+1/2$ defects and become depleted from $-1/2$ defects. In chaining bacterial biofilms, stress accumulation at $-1/2$ defects was found to induce a buckling instability that leads to sporulation [23]. Finally, in epithelial monolayers, increased pressure around $+1/2$ defects was found to induce cell apoptosis and extrusion [19]. However, whether these or similar defect-induced processes serve any beneficial physiological

function remains unclear.

We find that topological defects play an important role in the developmental cycle of *M. xanthus*: they promote the layering processes that leads to fruiting body formation. By identifying and tracking topological defects (Fig. 3a, Movie S5, Methods), we found events in which new cell layers form close to $+1/2$ defects (Figs. 3b and 3c), and new holes open close to $-1/2$ defects (Figs. 3d and 3e). To quantify this relationship, we measured the distribution of distances between defects of either sign and the locations where new layers and new holes appear. These measurements indicate that it is ≈ 80 times more likely for a new layer to form close to a $+1/2$ defect than away from it (Fig. 3f), and that it is ≈ 110 times more likely for a new hole to open at a $-1/2$ defect than away from it (Fig. 3g).

To understand the association between topological defects and layering, we modeled the cell colony as a thin film of active nematic fluid (Supplementary Text). We describe cell alignment in terms of the nematic order parameter tensor field $\mathbf{Q}(\mathbf{r})$, which we assume relaxes rapidly to its equilibrium configuration. As cells migrate along the alignment axis, they mechanically interact with neighboring cells, which produces an anisotropic active stress $\sigma^{\mathrm{a}} = -\zeta\mathbf{Q}$ in the colony. The coefficient ζ is positive (negative) for extensile (contractile) stresses. The distortions of cell alignment found around topological defects give rise to a non-zero active force density $\mathbf{f}^{\mathrm{a}} = \nabla \cdot \sigma^{\mathrm{a}}$, which drives cell flows $\mathbf{v}(\mathbf{r})$ [28]. The active forces are balanced by viscous friction forces $\xi\mathbf{v}$ arising from cell-substrate interactions:

$$\xi\mathbf{v} = \mathbf{f}^{\mathrm{a}}. \tag{1}$$

Like the active stresses, we assume that friction forces are anisotropic. Following Ref. [18], we account for friction anisotropy via a friction coefficient matrix $\xi = \xi_0\left[\mathbb{I} - \epsilon\,\mathbf{Q}\right]$, where the first term corresponds to isotropic friction with coefficient ξ_0, and ϵ is the friction anisotropy along the local alignment axis. Previous measurements of the mechanical response of cell-substrate focal adhesions in *M. xanthus* [29] suggest that friction is smaller along the cell-alignment axis than perpendicular to it, i.e. $\epsilon > 0$.

Assuming equilibrium solutions for the order parameter $\mathbf{Q}(\mathbf{r})$ around topological defects, we solved Eq. (1) to predict the cell flow fields around $+1/2$ and $-1/2$ defects (Supplementary Text). The results show that $+1/2$ defects exhibit net self-driven motion along their axis of symmetry (Fig. 4a), a well-known feature of active nematic fluids [8, 12, 13, 30–32]. Moreover, cells in front of the defect are aligned perpendicularly to the flow, thus experiencing stronger friction than cells behind the defect. Therefore, due to the positive friction anisotropy $\epsilon > 0$, the inflow toward the defect core is stronger than the outflow (Fig. 4a). As a result, cells accumulate at $+1/2$ defects, and are eventually extruded vertically to form new cell layers (Figs. 3b and 3c). For $-1/2$ defects, anisotropic friction gives rise to a stronger outflow than inflow (Fig. 4b), which explains the opening of holes at $-1/2$ defects (Figs. 3d and 3e). Were friction isotropic, the velocity field around defects would be symmetric, implying no cell accumulation or depletion, and hence no layer formation or hole
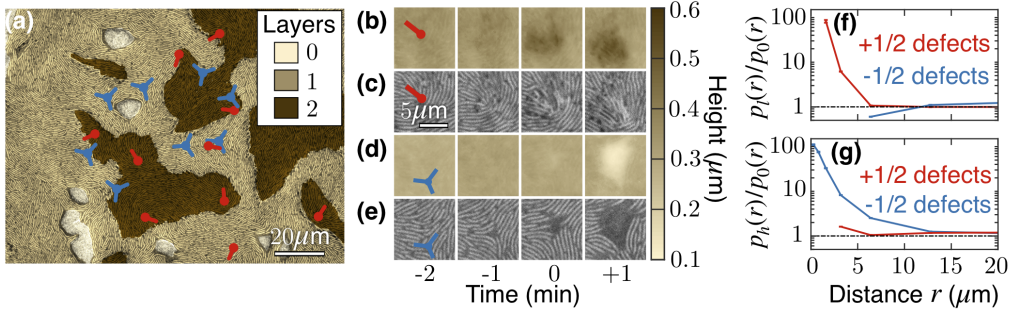
Figure 3: New layers and new holes preferentially form at $+1/2$ **and** $-1/2$ **topological defects, respectively.** (**a**) Layer-count field overlaid on a reflectance image of the bacterial colony. $+1/2$ and $-1/2$ defects are marked with red and blue symbols, respectively. Snapshots of the height and the reflectance fields for both a layer-formation event at a $+1/2$ defect (**b**, **c**), and a hole-opening event at a $-1/2$ defect (**d**, **e**). Probability distributions of the distance between defects and new layers (**f**), and between defects and new holes (**g**). The distributions are normalized by the distribution of distances between defects and randomly selected points. Therefore, the plots indicate how much more likely it is for new layers and holes to appear at a given distance from $+1/2$ and $-1/2$ defects.

opening.

To test our predictions, we measured cell flows around topological defects by calculating optical flow from the reflectance movies (Methods). In agreement with our theoretical predictions, the measured flow fields show that $+1/2$ defects self-propel along their axis, and that there is a net inflow toward $+1/2$ defects (Fig. 4c), while there is a net outflow from $-1/2$ defects (Fig. 4d). Also in agreement with our predictions, we find that cell accumulation ($\nabla \cdot \mathbf{v} < 0$) occurs mainly in front of $+1/2$ defects, whereas cell depletion ($\nabla \cdot \mathbf{v} > 0$) is localized in three lobes along the axes of symmetry of $-1/2$ defects (Fig. S4).

To quantitatively assess our model, we fit the theoretical predictions to the measured velocity profile along the midline of topological defects, i.e. $v_x(x, y = 0)$ (Fig. 4e, Supplementary Text). The fits yield values for three model parameters: the nematic healing length ℓ that determines the defect core size, the ratio ζ/ξ_0 between active stress and isotropic friction coefficients, and the friction anisotropy ϵ (Table I). For both $+1/2$ and $-1/2$ defects, we obtain $\ell \approx 2.5$ μm; the defect core is smaller than a cell length $l \approx 7$ μm. In addition, we find that active stress in the bacterial colony is extensile ($\zeta > 0$), and that friction anisotropy is positive ($\epsilon > 0$). However, the optimal values of ζ/ξ_0 and ϵ are different for $+1/2$ and $-1/2$ defects, suggesting that cells experience a different effective friction around each defect type, likely due to the distinct mechanical details of the layer formation and the hole opening processes.

For $-1/2$ defects, the fit (blue curve) closely matches the data (grey points, Fig. 4e). However, in front of $+1/2$ defects, the fit (red curve) qualitatively departs from the data (black points, Fig. 4e). Whereas for $+1/2$ defects our model predicts a negative velocity $v_x < 0$ everywhere along the defect midline, we measure a positive velocity $v_x > 0$ for $x \lesssim -10$ μm (Fig. 4e), indicating that cells in this region flow toward the defect core, opposite to the overall motion of the defect. In the following, we propose a possible explanation for this observation. Our model so far assumed that, under compression, cells are readily extruded from the cell monolayer. Accord-

ingly, we assumed that the cell density is uniform ($\rho(\mathbf{r}) = \rho_0$) and, hence, we neglected pressure gradients in Eq. (1). However, if cells are not readily extruded, the non-uniform flows around a $+1/2$ defect produce compression in the cell monolayer, leading to a pressure increase in front of $+1/2$ defects. The resulting pressure gradient drives an additional flow toward the defect core, which might account for the measured net counterflow. To probe this idea, we generalized our active nematic model to allow for a non-uniform cell density $\rho(\mathbf{r})$ and the associated pressure gradients (Supplementary Text). The force balance then reads

$$\xi\mathbf{v} = -\nabla P(\rho) + \mathbf{f}^{\mathrm{a}}, \qquad (2)$$

and we assume a linear equation of state $P(\rho) = B\left[\rho - \rho_0\right]/\rho_0 + P(\rho_0)$, where B is the bulk modulus of the monolayer. With additional assumptions about the rate of cell extrusion (Supplementary Text), this extended model produces counterflow, as shown by the fit of the predicted midline velocity (yellow curve in Fig. 4e, Supplementary Text). Gaining further insight into the physical origin of the counterflow will require future experiments that can accurately measure the cell density and mechanical stress around defects.

In summary, a dense monolayer of *M. xanthus* cells migrating on a surface forms an active nematic liquid crystal. Spontaneously-created topological defects of the liquid-crystalline alignment induce the formation of new cell layers and holes in the bacterial colony. The localization of these layering events at topological defects results from the anisotropic friction that the cells experience as they migrate. Thus, we propose that cell motility and mechanical interactions between cells are sufficient to drive the formation of multilayered structures, which lead to fruiting bodies in *M. xanthus*. Upon starvation, *M. xanthus* cells might alter their motility to drive aggregation of the colony [5]. Once aggregated in dense monolayers, we have shown that cells may form new layers as a result of self-organized mechanical processes that spontaneously occur in collections of self-propelled rods. Future work will be needed to connect starvation-induced changes in motility to the growth of fully-developed, stable fruiting bodies.
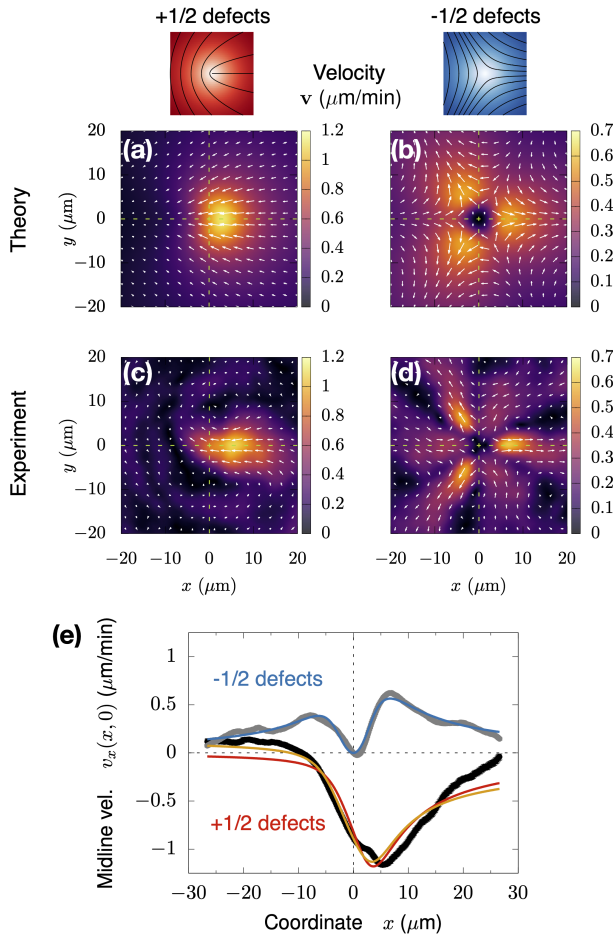
Figure 4: Asymmetric cell flows around topological defects explain the formation of new layers and holes. The defect schematics show the order parameter (color map) along with director-field lines. Theoretically predicted (**a**, **b**) and experimentally measured (**c**, **d**) flow fields around topological defects. The color maps indicate the speed, and the white arrows indicate the velocity. The defect cores are located at the origin of coordinates, with the green dashed lines indicating the coordinate axes. The net influx of cells at $+1/2$ defects and the net outflux from $-1/2$ defects lead to the formation of new layers and new holes, respectively. (**e**) Fits of the theoretical predictions to the experimentally measured velocity profiles along the midline ($y = 0$) of $+1/2$ (black data points and red fitted curve) and $-1/2$ (grey data points and blue fitted curve) defects. The optimal values of the fitting parameters, which were used to plot panels **a** and **b**, are listed in Table I. The yellow curve is the fit of the extended model that accounts for the counterflow measured in front of $+1/2$ defects, in the region $x \lesssim -10\ \mu$m. The corresponding optimal parameter values are listed in Table II.

Finally, the formation of multilayered cell structures from an initial cell monolayer is not unique to *M. xanthus*: it occurs both in biofilms of other bacterial species [33, 34], as well as in the stratification of the mammalian epidermis [35]. Even though the precise cellular mechanisms may differ in different systems, it is appealing to speculate that population-scale orientational order and the associated topological defects may provide a generic route to the formation of cell layers in a wide range of biological systems.

AUTHOR CONTRIBUTIONS

K.C. performed the experiments and analyzed the data. R.A. developed the theory and fitted the predictions to the experimental data. All authors interpreted the results and designed experiments. N.S.W. and J.W.S. supervised the study. K.C. and R.A. wrote the manuscript with input from all authors.

COMPETING INTERESTS

The authors declare no competing interests.

DATA AND MATERIALS AVAILABILITY

All data are available from the authors upon request.

[1] D. Kaiser, Nat. Rev. Microbiol. **1**, 45 (2003).

[2] Y. Zhang, A. Ducret, J. Shaevitz, and T. Mignot, FEMS Microbiol. Rev. **36**, 149 (2012).

[3] S. K. Kim and D. Kaiser, Science **249**, 926 (1990).

[4] L. Jelsbak and L. Søgaard-Andersen, Proc. Natl. Acad. Sci. U. S. A. **99**, 2032 (2002).

[5] G. Liu, A. Patch, F. Bahar, D. Yllanes, R. D. Welch, M. C. Marchetti, S. Thutupalli, and J. W. Shaevitz, Phys. Rev. Lett. **122**, 248102 (2019).

[6] P. D. Curtis, R. G. Taylor, R. D. Welch, and L. J. Shimkets, J. Bacteriol. **189**, 9126 (2007).

[7] D. Kaiser and H. Warrick, Proc. Natl. Acad. Sci. U. S. A. **111**, 13105 (2014).

[8] A. Doostmohammadi, J. Ignés-Mullol, J. M. Yeomans, and F. Sagués, Nat. Commun. **9**, 3246 (2018).

[9] M. C. Marchetti, J. F. Joanny, S. Ramaswamy, T. B. Liverpool, J. Prost, M. Rao, and R. A. Simha, Rev. Mod. Phys. **85**, 1143 (2013).

[10] M. Bär, R. Großmann, S. Heidenreich, and F. Peruani, Annu. Rev. Condens. Matter Phys. **11**, 441 (2020).

[11] P.-G. de Gennes and J. Prost, *The Physics of Liquid Crystals*, 2nd ed. (Oxford University Press, 1993).

[12] L. Giomi, M. J. Bowick, X. Ma, and M. C. Marchetti, Phys. Rev. Lett. **110**, 228101 (2013).

[13] X.-Q. Shi and Y.-Q. Ma, Nat. Commun. **4**, 3013 (2013).

[14] V. Narayan, S. Ramaswamy, and N. Menon, Science **317**, 105 (2007).

[15] T. Sanchez, D. T. N. Chen, S. J. DeCamp, M. Heymann, and Z. Dogic, Nature **491**, 431 (2012).

[16] N. Kumar, R. Zhang, J. J. de Pablo, and M. L. Gardel, Sci. Adv. **4**, eaat7779 (2018).

[17] G. Duclos, C. Erlenkämper, J.-F. Joanny, and P. Silberzan, Nat. Phys. **13**, 58 (2017).

[18] K. Kawaguchi, R. Kageyama, and M. Sano, Nature **545**, 327 (2017).

[19] T. B. Saw, A. Doostmohammadi, V. Nier, L. Kocgozlu, S. Thampi, Y. Toyama, P. Marcq, C. T. Lim, J. M. Yeomans, and B. Ladoux, Nature **544**, 212 (2017).

[20] C. Blanch-Mercader, V. Yashunsky, S. Garcia, G. Duclos, L. Giomi, and P. Silberzan, Phys. Rev. Lett. **120**, 208101 (2018).

[21] A. Doostmohammadi, S. P. Thampi, and J. M. Yeomans, Phys. Rev. Lett. **117**, 048102 (2016).

[22] D. Dell'Arciprete, M. L. Blow, A. T. Brown, F. D. C. Farrell, J. S. Lintuvuori, A. F. McVey, D. Marenduzzo, and W. C. K. Poon, Nat. Commun. **9**, 4190 (2018).

[23] Y. I. Yaman, E. Demir, R. Vetter, and A. Kocabas, Nat. Commun. **10**, 2285 (2019).

[24] H. Li, X.-Q. Shi, M. Huang, X. Chen, M. Xiao, C. Liu, H. Chaté, and H. P. Zhang, Proc. Natl. Acad. Sci. U. S. A. **116**, 777 (2019).

[25] T. B. Saw, W. Xi, B. Ladoux, and C. T. Lim, Adv. Mater. **30**, 1802579 (2018).

[26] C. Peng, T. Turiv, Y. Guo, Q.-H. Wei, and O. D. Lavrentovich, Science **354**, 882 (2016).

[27] M. M. Genkin, A. Sokolov, O. D. Lavrentovich, and I. S. Aranson, Phys. Rev. X **7**, 011029 (2017).

[28] Because the height of the fluid layer can change freely, the two-dimensional velocity field $\mathbf{v}(\mathbf{r})$ can have a non-zero divergence, $\nabla \cdot \mathbf{v} \neq 0$ (see Eq. (S11) in the Supplementary Text).

[29] R. Balagam, D. B. Litwin, F. Czerwinski, M. Sun, H. B. Kaplan, J. W. Shaevitz, and O. A. Igoshin, PLoS Comput. Biol. **10**, e1003619 (2014).

[30] L. Giomi, M. J. Bowick, P. Mishra, R. Sknepnek, and M. C. Marchetti, Philos. Trans. A. Math. Phys. Eng. Sci. **372**, 20130365 (2014).

[31] L. M. Pismen, Phys. Rev. E. Stat. Nonlin. Soft Matter Phys. **88**, 050502 (2013).

[32] S. Shankar, S. Ramaswamy, M. C. Marchetti, and M. J. Bowick, Phys. Rev. Lett. **121**, 108002 (2018).

[33] A. Shrivastava, V. K. Patel, Y. Tang, S. C. Yost, F. E. Dewhirst, and H. C. Berg, Proc. Natl. Acad. Sci. U. S. A. **115**, 8633 (2018).

[34] Z. You, D. J. G. Pearce, A. Sengupta, and L. Giomi, Phys. Rev. Lett. **123**, 178001 (2019).

[35] Y. A. Miroshnikova, H. Q. Le, D. Schneider, T. Thalheim, M. Rübsam, N. Bremicker, J. Polleux, N. Kamprad, M. Tarantola, I. Wang, M. Balland, C. M. Niessen, J. Galle, and S. A. Wickström, Nat. Cell Biol. **20**, 69 (2018).

[36] O. Vincent and O. Folorunso, in *Proceedings of the Informing Science & IT Education Conference* (2009).

[37] R. M. Haralick and L. G. Shapiro, *Computer and Robot Vision* (Addison-Wesley, Boston, 1992).

[38] A. J. Vromans and L. Giomi, Soft Matter **12**, 6490 (2016).

[39] B. D. Lucas and T. Kanade, in *Proceedings of the DARPA Image Understanding Workshop* (1981) pp. 121–130.

[40] A. N. Beris and B. J. Edwards, *Thermodynamics of Flowing Systems with Internal Microstructure* (Oxford University Press, 1994).

[41] J. V. Selinger, *Introduction to the Theory of Soft Matter. From Ideal Gases to Liquid Crystals* (Springer, 2016).

[42] S. Ramaswamy, R. A. Simha, and J. Toner, Europhys. Lett. **62**, 196 (2003).

[43] F. Jülicher, S. W. Grill, and G. Salbreux, Reports Prog. Phys. **81**, 076601 (2018).

[44] L. M. Pismen, *Patterns and interfaces in dissipative dynamics* (Springer, 2006).

[45] L. M. Pismen, *Vortices in Nonlinear Fields. From Liquid Crystals to Superfluids. From Non-Equilibrium Patterns to Cosmic Strings* (Oxford University Press, 1999).

MATERIALS AND METHODS

Cell culture

Myxococcus xanthus cells of the wild-type strain DK1622 are grown in CTTYE (1% Casitone, 10 mM Tris-HCl [pH = 7.6], 1 mM KH_2PO_4, 8 mM $MgSO_4$) overnight to a concentration corresponding to a range of $OD_{600} \approx 0.4 - 0.8$, where OD_{600} is the optical density at a wavelength of 600 nm. This culture is then concentrated and re-suspended into fresh CT-TYE to an $OD_{600} \approx 2$. Then, 5 μl of concentrated culture is placed onto a CTTYE pad with 1.5% agarose, and allowed to dry until no liquid is visible on the surface of the agarose gel. Next, the sample is incubated for 2 hours before imaging.

Imaging

We image our samples using a Keyence VK-X 1000 microscope. The microscope works by scanning a laser across the surface of the sample and measuring the reflectance of the laser light on the surface. The reflectance of the sample is measured at multiple heights. Then, a height field of the sample (Fig. 1c) is obtained by finding, for each pixel, the height at which the reflectance is maximal. Finally, the reflectance field at the height of maximal reflectance gives clear and in-focus images of the top of sample (Fig. 1a). Imaging was done at a frame rate between 4.8 and 7.2 $\min^{-1}$ for 1 to 3 hours.

Cell motility measurements and state of the colony

M. xanthus colonies undergo a transition from a non-aggregated state in which the colony forms a thin film on the agar substrate to an aggregated state that leads to fruiting body formation. A recent study has shown that this transition is controlled by a dimensionless number known as the inverse rotational Péclet number,

$$\text{Pe}_r^{-1} = \frac{\ell_{cell}}{v_0}(D_r + 2f_{rev}), \quad (S1)$$

which combines the effects of the cells' self-propulsion speed v_0, their rotational diffusion coefficient D_r, and the average rate of velocity reversals f_{rev} [5]. $\ell_{cell} = 2.5$ μm is an effective average cell size [5]. Here, in order to study layer formation, we maintain the cell colony in the regime of cell migration parameters corresponding to the non-aggregated state. To check that our experiments lie within the appropriate parameter regime, we tracked cells moving at a low cell density corresponding to an $OD_{600} = 0.1$, and we measured the probability distribution of cell speeds and of times between velocity-reversal events (Fig. S1). We find that cells move with an average speed $v_0 = 0.922 \pm 0.009$ $\mu m/min$, and an
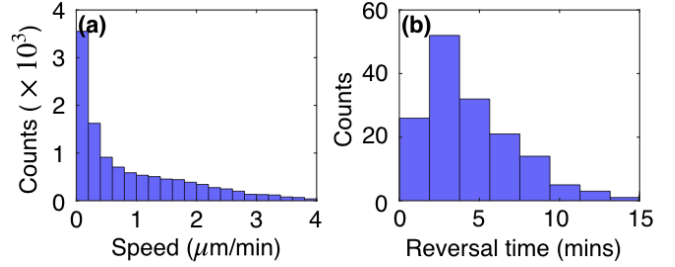

Figure S1: Properties of *M. xanthus* motility. Histograms of the cell speed (**a**) and time between velocity reversals (**b**) of cells migrating in a low-cell-density environment.

average reversal rate $f_{rev} = 0.172 \pm 0.002$ $\min^{-1}$. The value of the rotational diffusion coefficient, $D_r = 0.127$ $\min^{-1}$, was taken from Ref. [5]. These motility parameter values give $\text{Pe}_r^{-1} = 1.28 \pm 0.09$, which lies well within the non-aggregated state in the phase diagram of Ref. [5].

Layer number

To obtain the number of layers at each point in the cell colony, we first detect height gradients by applying a Sobel filter [36] to the measured height fields. This way, we identify edges of potential cell layers. Often, the detected edges are not continuous but feature gaps. To close these gaps, we first dilate and then erode the detected edges [37]. Compact regions of the image between the detected edges are candidates to be identified as a cell layer. To assign a layer count to these candidate regions, we first find the largest candidate region and assign it a layer count of 1, i.e. we assume that the largest candidate layer corresponds to the basal cell monolayer. Next, for any other candidate layer (for example, green region in Fig. S2a), we calculate the height difference Δh between its average height and the average height of the portions of other candidate regions that are within an in-plane distance of 5 μm (for example, red region in Fig. S2a). This way, we calculate the height difference between all pairs of candidate regions, and we build the histogram shown in Fig. S2b. The central peak of this histogram shows that a large subset of the pairs of candidate regions have small height differences between them, indicating that they have the same layer count. However, the secondary peaks at $\Delta h \neq 0$ (Fig. S2b) correspond to pairs of candidate regions with a step up or down in layer count between them. Based on these secondary peaks of the height-differences distribution, for each experiment, we select a different threshold Δh_c in the range $0.08 \sim 0.2$ μm above which candidate regions are considered to have different layer counts. We then compare the average height of each candidate region to any portions of previously-labeled regions within 5
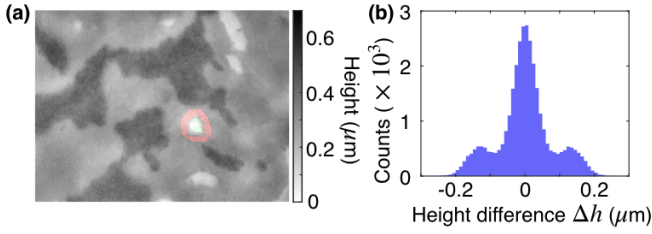
Figure S2: Layer number fields. (**a**) Example of two neighboring candidate cell layers (green and red) identified by applying an edge-detection algorithm to the measured height fields. (**b**) The histogram of height differences Δh between the average height of all pairs of neighboring candidate regions. The peaks at $\Delta h \neq 0$ correspond to pairs of candidate regions with different cell layer count.
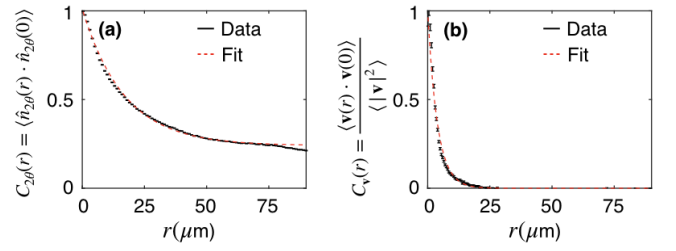

Figure S3: Correlation functions. Spatial correlation functions of (**a**) the modified director field $\hat{n}_{2\theta} = (\cos(2\theta), \sin(2\theta))$, and (**b**) of the velocity field $\mathbf{v}$. By fitting exponential decays, we obtain the nematic and the velocity correlation lengths: $\ell_n = 16.0 \pm 0.5~\mu$m, and $\ell_v = 3.9 \pm 0.1~\mu$m, respectively.

μm and assign a layer count to the candidate region accordingly. Once all candidate regions have been assigned a layer count, we proceed to assign a layer count also to the edge regions. To each pixel of the detected edges, we assign the layer count of the layer with the closest height value in connected regions within $5~\mu$m. From the obtained layer-count fields, we subtract the lowest layer count to ensure that the agarose substrate is labeled with a layer count of 0. Finally, we visually check all layer number fields and make minimal necessary corrections manually. The layer number fields obtained using this procedure are shown in Fig. 1d and in Movie S5.

Nematic order

To characterize the nematic order in the cell colony, we measure the orientation angle field $\theta(\mathbf{r}, t)$ and the nematic order parameter strength field $S(\mathbf{r}, t)$ from the laser brightness images of the colony. Following Ref. [24], we first sharpen the laser-brightness signal by means of a high-pass filter. Then, we compute the gradient of the resulting brightness field I_{ij}, where the indices indicate the image pixels. We smooth the brightness gradient by means of a Gaussian filter with standard deviation $\sigma = 1.7~\mu$m. Then, for each pixel, we build the so-called structure tensor

$$H_{ij} = \begin{pmatrix} (\partial_x I_{ij})^2 & (\partial_x I_{ij})(\partial_y I_{ij}) \\ (\partial_x I_{ij})(\partial_y I_{ij}) & (\partial_y I_{ij})^2 \end{pmatrix}, \quad \text{(S2)}$$

and we obtain its eigenvalues and eigenvectors. The eigenvector associated with the smallest eigenvalue gives the local direction of least brightness gradient, which we identify with the angle field θ_{ij} of cell orientation.

From the measured angle field θ_{ij}, we obtain the order parameter strength field S_{ij} as [11]

$$S_{ij} = \langle 2\cos(\theta_{ij} - \bar{\theta}_{ij}) - 1 \rangle_R, \quad \text{(S3)}$$

where $\bar{\theta}_{ij} = \langle \theta_{ij} \rangle_R$ is the average orientation angle within a disk of radius $R = 1~\mu$m centered at pixel (i, j). S_{ij} is almost 1 over the majority of the system, indicating an almost

perfect cell alignment, but it approaches 0 at defects, where cell alignment is lost and the angle field is singular (Fig. 2b).

Following Ref. [24], we measure the following spatial correlation function of the nematic orientation angle,

$$C_{2\theta}(r) = \langle \hat{n}_{2\theta}(r) \cdot \hat{n}_{2\theta}(0) \rangle, \quad \text{(S4)}$$

where $\hat{n}_{2\theta} = (\cos(2\theta), \sin(2\theta))$. The average runs over 10000 randomly-selected pairs of points from every frame of every experiment. We fit an exponential decay with an offset $C_{2\theta}(r) = A\,e^{-r/\ell_n} + B$ to the measured correlation function (Fig. S3a) and obtain the nematic correlation length $\ell_n = 16.0 \pm 0.5~\mu$m.

Finally, to measure the equilibrium value of the order parameter strength, S_0 (see Supplementary Text), we obtain the average $S_0 = \langle S(\mathbf{r}, t) \rangle$ over regions of the cell colony without defects. Specifically, we exclude circular regions of radius $R_{\text{def}} = 16~\mu\text{m} \approx \ell_n$ around topological defects (see below for a description of the defect detection method). In addition, we also exclude holes in the cell colony, i.e. regions without cells. Using this procedure, we obtain $S_0 = 0.992 \pm 0.003$.

Defect detection and tracking

We identify and track defects by finding local minima of the nematic order parameter strength $S(\mathbf{r}, t)$ with $S < 0.7$. Often, several pixels around these local minima have the same value of S. Thus, we identify the defect core with the centroid of all the pixels that share the local minimum value of S.

For each point identified as a potential defect core, we calculate the topological charge q by applying its definition:

$$q = \frac{1}{2\pi} \oint_{\mathcal{C}} d\theta, \quad \text{(S5)}$$

where $\mathcal{C}$ is a circular circuit of radius $R_c = 1~\mu$m around the defect core. We ignore the candidate points with $q = 0$, as well as the ones that fall in holes in the cell colony.

For each defect, we identify its axes of symmetry as recently proposed in Ref. [38]. Specifically, for defects with topological charge $+1/2$, the defect axis is given by $\hat{p} =$
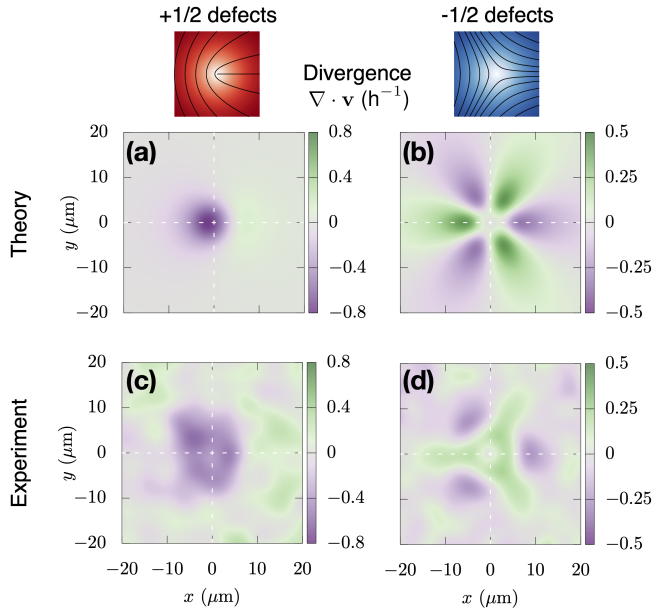
Figure S4: Divergence of the flow field. Theoretically predicted (**a**, **b**) and experimentally measured (**c**, **d**) divergence fields around topological defects. The defect schematics show the order parameter (color map) and a few director-field lines. The divergence of the two-dimensional flow field, $\nabla \cdot \mathbf{v}$, shows pronounced cell accumulation ($\nabla \cdot \mathbf{v} < 0$, purple) in front of $+1/2$ defects, and cell depletion ($\nabla \cdot \mathbf{v} < 0$, green) in three lobes along the axes of symmetry of $-1/2$ defects. The parameter values used to plot panels **a** and **b** are listed in Table I.

$\nabla \cdot \mathbf{Q}/|\nabla \cdot \mathbf{Q}|$, where $\mathbf{Q}$ is the nematic order parameter tensor with components $Q_{\alpha\beta} = S[2\hat{n}_\alpha \hat{n}_\beta - \delta_{\alpha\beta}]$, with $\hat{n} = (\cos\theta, \sin\theta)$ the director field. Respectively, for defects with topological charge $-1/2$, we first define the opposite nematic angle $\theta' = -\theta$, and we obtain the corresponding $\mathbf{Q}'$ tensor. From it, we obtain $\hat{p}' = \nabla \cdot \mathbf{Q}'/|\nabla \cdot \mathbf{Q}'|$. Finally, defining $\hat{p}' = (\sin\psi', \cos\psi')$, one symmetry axis of a $-1/2$ defect is given by the angle $\psi = -\psi'/3$. The other two symmetry axes of a $-1/2$ defect are then defined by the three-fold symmetry of $-1/2$ defects.

Finally, we track defects over time by finding the closest defects with the same charge in consecutive image frames. We ignore defects that last less than 10 frames (≈ 2 min). Across eight individual experiments, we found 96 defects with a topological charge of $q = +1/2$ and 144 defects with $q = -1/2$. All together, the $+1/2$ defect tracks consist of a total of

3168 defect frames, which are included in the averaged data in Figs. 2d and 4c. Respectively, a total of 3688 $-1/2$ defect frames are included in the averaged data in Figs. 2e and 4d.

Cell flow measurements

We measure cell flows by applying an optical-flow algorithm on the laser-brightness images of the cell colony. The optical-flow algorithm is based on the Lucas-Kanade derivative of Gaussian method [39]. By comparing independent velocity measurements from a small number of manual cell trackings to the optical-flow measurements, we find a calibration parameter to convert the optical flow to a cell velocity field within the bacterial colony.

Finally, we measure the spatial correlation function of the velocity field:

$$C_{\mathrm{v}}(r) = \frac{\langle \mathbf{v}(r) \cdot \mathbf{v}(0) \rangle}{\langle |\mathbf{v}|^2 \rangle}. \tag{S6}$$

As for the nematic correlation function Eq. (S4), the average runs over 10000 randomly-selected pairs of points from every frame of every experiment. We fit an exponential decay $C_{\mathrm{v}}(r) = D\, e^{-r/\ell_{\mathrm{v}}}$ to the measured correlation function (Fig. S3b) and obtain the velocity correlation length $\ell_{\mathrm{v}} = 3.9 \pm 0.1\ \mu$m.

SUPPLEMENTARY MOVIES

Movie S1. Reflectance field of a thin cell colony, with new holes and cell layers appearing and disappearing.

Movie S2. Height field corresponding to Movie S1.

Movie S3. Color map of the cell orientation angle θ overlaid on a magnified reflectance movie of the colony.

Movie S4. Nematic alignment field S of the colony.

Movie S5. Red and blue symbols track the positions and orientations of $+1/2$ and $-1/2$ topological defects, respectively, as they spontaneously appear, move, and annihilate within the cell colony. The color map shows the number of layers overlaid on a laser-brightness movie of the colony. The color code is as in Fig. 1d.

SUPPLEMENTARY TEXT

A. Active nematic model of the bacterial colony

In this section, we model a monolayer of *Myxococcus xanthus* cells as an active nematic fluid. The cell monolayer forms a phase with nematic liquid-crystalline order as a result of the dense packing and rod-like shape of *M. xanthus* cells. The nematic nature of the ordering is confirmed by the presence of topological defects with half-integer topological charge, which are only possible in systems with nematic symmetry. The activity of the colony stems from cell migration: *M. xanthus* cells exert traction forces on the substrate to self-propel along their long axis. As cells move in the dense colony, they mechanically interact with neighboring cells. These mechanical interactions give rise to active stresses in the cell monolayer. The presence of active stresses is evidenced by the self-propulsion of $+1/2$ topological defects, which is a fingerprint of active nematic systems [8]. As they move, cells continuously slide past each other, rearranging and exchanging neighbors in the colony. Thus, the colony is in a fluid state. Altogether, we conclude that the bacterial colony forms an active nematic fluid layer. In the following, we present a minimal continuum model to describe the flows of cells in this bacterial monolayer.

1. Nematic order

Based on the physics of liquid crystals [11], we describe the orientational order of the cell monolayer in terms of the nematic order-parameter tensor $\mathbf{Q}$. In two dimensions, $Q_{\alpha\beta} = S[2\hat{n}_\alpha\hat{n}_\beta - \delta_{\alpha\beta}]$, where S is the scalar strength of the order parameter, and $\hat{n} = (\cos\theta, \sin\theta)$ is the unitary director field, with θ the orientation angle. The cartesian components of $\mathbf{Q}$ are therefore

$$Q_{xx} = -Q_{yy} = S\cos(2\theta), \tag{S7a}$$
$$Q_{xy} = Q_{yx} = S\sin(2\theta). \tag{S7b}$$

In terms of $\mathbf{Q}$, we write the nematic free energy as [40, 41]

$$F = \int \left[\frac{a}{2}Q_{\alpha\beta}Q_{\alpha\beta} + \frac{b}{4}(Q_{\alpha\beta}Q_{\alpha\beta})^2 \right.$$
$$\left. + \frac{L}{2}(\partial_\alpha Q_{\beta\gamma})(\partial_\alpha Q_{\beta\gamma}) \right] \mathrm{d}^2\vec{r}. \tag{S8}$$

The first two terms come from a Landau expansion in the order parameter, with $a < 0$ in the nematic phase, and $b > 0$ for stability. These coefficients define the saturation value of the order parameter strength, $S_0 = \sqrt{-a/(2b)}$. The last term corresponds to the Frank energy, which accounts for the orientational elasticity of liquid crystals. We have taken the usual one-constant approximation, where L is the single orientational elastic modulus of the material, which is directly related to the Frank elastic constant K [11, 40, 41].

For simplicity, we ignore flow-alignment couplings, which only result in a small correction to the self-propulsion speed of $+1/2$ defects [32]. Moreover, we assume that the nematic relaxation rate is much faster than the typical strain rates associated with the flows. In this limit [30, 32], the order-parameter field relaxes to the configuration that minimizes the free energy Eq. (S8), i.e.

$$\frac{\delta F}{\delta Q_{\alpha\beta}} = (a + b\,Q_{\gamma\delta}Q_{\gamma\delta})\,Q_{\alpha\beta} - L\nabla^2 Q_{\alpha\beta} = 0. \tag{S9}$$

Given that $\mathbf{Q}$ is a rank-2 symmetric and traceless tensor, it can be described in terms of a single complex field $\psi = Q_{xx} + iQ_{xy} = S\,e^{2i\theta}$. In terms of this field, the equilibrium condition Eq. (S9) reads

$$L\nabla^2\psi = \left(a + 2b|\psi|^2\right)\psi, \tag{S10}$$

whose solution determines the nematic order in the system.

2. Force balance

We treat the cell monolayer as a thin layer of an incompressible fluid with an upper free boundary described by the height profile $h(\mathbf{r}, t)$, where $\mathbf{r}$ is the two-dimensional position vector. The incompressibility condition imposes $\nabla \cdot \mathbf{u} = 0$ on the three-dimensional flow field $\mathbf{u}$. Choosing the $\hat{z}$ axis perpendicular to the plane, and decomposing the velocity field into in-plane and out-of-plane components, $\mathbf{u} = (\mathbf{v}, u_z)$, the incompressibility condition can be recast as

$$\partial_t h(\mathbf{r}, t) = -\nabla \cdot \int_0^{h(\mathbf{r},t)} \mathbf{v}(\mathbf{r}, z, t)\,\mathrm{d}z. \tag{S11}$$

This equation expresses that the divergence of the planar flow field gives rise to height changes of the fluid layer.

Following previous work [18], we initially neglect planar pressure gradients in the force balance. This corresponds to assuming that, under compression, cells in one layer do not build up pressure because they can readily move to another layer. This assumption will be relaxed in Section C. Moreover, we treat the cell colony as a dry system [9, 42], i.e. we neglect internal viscous forces with respect to cell-substrate friction. This approximation is well justified based on the experimentally measured correlation length of the velocity field, $\ell_v = 3.9 \pm 0.1$ μm (Fig. S3b). This correlation length is smaller than the nematic correlation length $\ell_n = 16.0 \pm 0.5$ μm (Fig. S3a), and even smaller than the length of a single cell, $l \approx 7$ μm. Therefore, long-range hydrodynamic interactions can be safely neglected in this system. Furthermore, because we assume that the nematic order parameter rapidly relaxes to its equilibrium configuration (Eq. (S9)), both the antisymmetric and the flow-alignment contributions to the stress tensor vanish [43]. With these simplifications, the force balance reduces to a balance between frictional and active forces in the nematic cell monolayer:

$$\xi_{\alpha\beta}v_\beta = f_\alpha^{\mathrm{a}}. \tag{S12}$$

Here, $f_\alpha^{\mathrm{a}} = \partial_\beta\sigma_{\alpha\beta}^{\mathrm{a}}$ is the active force density that arises from the anisotropic active stress $\sigma_{\alpha\beta}^{\mathrm{a}} = -\zeta Q_{\alpha\beta}$ developed in the

colony, with coefficient $\zeta > 0$ for extensile and $\zeta < 0$ for contractile stresses. Finally, $\xi_{\alpha\beta}$ is the friction coefficient matrix.

To account for the anisotropy of cell-substrate interactions, we take [18]

$$\xi_{\alpha\beta} = \xi_0 \left[\delta_{\alpha\beta} - \epsilon \, Q_{\alpha\beta} \right]. \tag{S13}$$

Here, the first term accounts for isotropic friction with coefficient ξ_0, whereas the second term makes the friction coefficient depend on the local cell orientation via the nematic order parameter $Q_{\alpha\beta}$. Thus, ϵ is the friction anisotropy. For $\epsilon > 0$, friction is stronger in the direction perpendicular to the alignment of cells. Even though, to some extent, friction anisotropy might stem from the elongated shape of *M. xanthus* cells, its main source is likely the anisotropic response of cell-substrate focal adhesions. Previous experiments suggest that these adhesions barely yield in the direction perpendicular to the long cell axis, but are readily detached and reformed along the cell axis during gliding motility [29]. These observations suggest that $\epsilon > 0$ for *M. xanthus*.

B. Nematic order and flow fields around topological defects

In this section, we solve the model introduced in Section A to obtain the nematic order and cell flow fields around isolated topological defects in the cell monolayer. We consider only the lowest-energy topological excitations, i.e. point defects with topological charge $q = \pm 1/2$.

1. Nematic order

For $\pm 1/2$ defects, the orientation angle is given by $\theta = q\phi = \pm\phi/2$, where ϕ is the polar angle defined with respect to the defect's symmetry axis. Consequently, and assuming that $S(\mathbf{r}) = S(r)$, where r is the radial distance from the defect core, Eq. (S10) reduces to

$$S''(r) + \frac{1}{r}S'(r) - \frac{1}{r^2}S(r) = \frac{1}{\ell^2}\left[\frac{S^2(r)}{S_0^2} - 1\right]S(r), \tag{S14}$$

where we have defined the nematic healing length $\ell = \sqrt{L/|a|}$. With the conditions $S(0) = 0$ and $S(\infty) = S_0$, the solution to this nonlinear equation determines the radial profile of nematic order around a topological defect. The full solution cannot be obtained analytically, but it can be approximated by the following Padé approximant [44, 45]:

$$S(r) = S_0 f(r/\ell); \qquad f(x) \approx x\sqrt{\frac{0.34 + 0.07x^2}{1 + 0.41x^2 + 0.07x^4}}. \tag{S15}$$

Note that the nematic order-parameter profile $S(r)$ is the same for both positive and negative defects, which are only distinguished by their orientation-angle profiles $\theta(\phi) = \pm\phi/2$.

2. Flow field

Based on the solutions of the nematic order around topological defects obtained above, and using Eq. (S7), we obtain the active-force density $f_\alpha^{\mathrm{a}} = -\zeta \partial_\beta Q_{\alpha\beta}$. For a $+1/2$ defect, with $\theta = \phi/2$, the Cartesian components of the active-force density are

$$f_x^{\mathrm{a},+} = -\zeta\left[S'(r) + \frac{S(r)}{r}\right], \tag{S16a}$$

$$f_y^{\mathrm{a},+} = 0. \tag{S16b}$$

Using these expressions, we can solve the force balance, Eq. (S12), to obtain the velocity field around a $+1/2$ defect:

$$v_x^+(r,\phi) = -\frac{\zeta}{\xi_0}\left[S'(r) + \frac{S(r)}{r}\right]\frac{1 + \epsilon\, S(r)\cos\phi}{1 - \epsilon^2 S^2(r)}, \tag{S17a}$$

$$v_y^+(r,\phi) = -\frac{\zeta}{\xi_0}\left[S'(r) + \frac{S(r)}{r}\right]\frac{\epsilon\, S(r)\sin\phi}{1 - \epsilon^2 S^2(r)}. \tag{S17b}$$

Respectively, for a $-1/2$ defect, with $\theta = -\phi/2$, the active-force density reads

$$f_x^{\mathrm{a},-} = -\zeta\left[S'(r) - \frac{S(r)}{r}\right]\cos(2\phi), \tag{S18a}$$

$$f_y^{\mathrm{a},-} = \zeta\left[S'(r) - \frac{S(r)}{r}\right]\sin(2\phi). \tag{S18b}$$

Solving Eq. (S12), the velocity field around a $-1/2$ defect is given by

$$v_x^-(r,\phi) = -\frac{\zeta}{\xi_0}\left[S'(r) - \frac{S(r)}{r}\right] \times \\ \frac{[1 + \epsilon\, S(r)\cos\phi]\cos(2\phi) + \epsilon\, S(r)\sin\phi\sin(2\phi)}{1 - \epsilon^2 S^2(r)}, \tag{S19a}$$

$$v_y^-(r,\phi) = \frac{\zeta}{\xi_0}\left[S'(r) - \frac{S(r)}{r}\right]\frac{[2\cos\phi - \epsilon\, S(r)]\sin\phi}{1 - \epsilon^2 S^2(r)}. \tag{S19b}$$

3. Fits to experimental data

To compare our theoretical predictions to the measured flow fields, we fitted the predicted velocity profile along the midline of the defects, i.e. the symmetry line that defines the $\hat{x}$ axis. Along this axis, the velocity field is entirely longitudinal, $\mathbf{v}(x,0) = v_x(x,0)\,\hat{x}$, with $v_y(x,0) = 0$. Moreover, along the midline, polar coordinates become $r = |x|$ and $\phi = 0, \pi$ for the positive and negative sides of the $\hat{x}$ axis. Using these relations, we fit Eqs. (S17a) and (S19a) to velocity profiles along the midline of $+1/2$ and $-1/2$ defects, respectively. Equations (S17a) and (S19a) depend on four parameters: the saturation value S_0 of the nematic order parameter, the healing length ℓ, the ratio ζ/ξ_0 between the active stress and the isotropic friction coefficients, and the friction anisotropy ϵ. The first two parameters characterize the nematic order

around defects (Eq. (S15)), whereas the last two parameters are related to the force balance Eqs. (S12) and (S13). To perform the fits, we fixed the value of $S_0 = 0.992 \pm 0.003$, as given by experimental measurements (Methods), and we left ℓ, ζ/ξ_0, and ϵ as fitting parameters. The optimal parameter values are listed in Table I, and the fits are shown in Fig. 4e (red and blue curves for $+1/2$ and $-1/2$ defects, respectively).

Whereas the values of the healing length ℓ for $+1/2$ and $-1/2$ defects are compatible, the values of ζ/ξ_0 and ϵ are not. The difference in parameter values for $+1/2$ and $-1/2$ defects suggests that cells experience a different effective friction around each defect type. This difference may stem from the different mechanical details of the layer formation and hole opening processes, which are not accounted for in our minimal model. Therefore, explaining the difference in the parameter values that we obtain from the fits requires a more detailed model that we defer to future work.

Parameter	$+1/2$ defects	$-1/2$ defects
ℓ (μm)	2.5 ± 0.1	2.54 ± 0.02
ζ/ξ_0 (μm^2/min)	1.77 ± 0.09	4.65 ± 0.04
ϵ	0.80 ± 0.01	0.214 ± 0.006

Table I: Optimal values of parameters obtained by fitting the velocity profile along the defect midline.

C. Compressibility effects: explanation of the counterflow in front of $+1/2$ defects

$+1/2$ defects exhibit an overall active motion along their axis. This defect motion corresponds to the negative velocity ($v_x < 0$) that we measure along most of the defect axis (Fig. 4e). However, in the front of $+1/2$ defects, we measure a cell flow toward the defect core, opposite to the overall motion of the defect. This frontal counterflow corresponds to the measured positive velocity ($v_x > 0$) in the region $x \lesssim -10$ μm (Fig. 4e). This counterflow cannot be explained by the model in Sections A and B. That model predicts that the active force is negative $f_x^{a,+} < 0$ at every point around an isolated $+1/2$ defect. As a consequence, the velocity is also negative everywhere, and there is no counterflow.

In this section, we propose a possible explanation for the measured counterflow. We argue that the counterflow may stem from pressure gradients that we neglected in the force balance Eq. (S12) based on the assumption that, under compression, cells are readily extruded from the cell monolayer. If cells do not readily move to an upper layer, the non-uniform motion of a $+1/2$ defect generates bulk deformations in the cell monolayer. In particular, the front of the defect experiences compression, leading to a pressure increase. Therefore, a pressure gradient is established along the defect axis. This expectation is consistent with the pressure gradient measured along the axis of $+1/2$ defects in epithelial monolayers [19]. This pressure gradient, in turn, generates a flow toward the

lower pressures at the defect core, i.e. opposite to the active flow responsible for defect motion. Far from the defect core, where active forces are small, the pressure-driven counterflow may overcome the active flow, thus possibly explaining our experimental observation of counterflow. In the following, we minimally extend our model to implement these ideas and predict the counterflow.

1. Active nematic model with a non-uniform cell density

In Sections A and B, we assumed that the cell density in the basal cell monolayer was uniform, $\rho(\mathbf{r}) = \rho_0$. As a consequence, the pressure in the basal layer was also uniform. Hence, pressure gradients vanished, and the force balance reduced to Eq. (S12),

$$\xi_{\alpha\beta}v_\beta^0 = f_\alpha^a, \qquad (S20)$$

where f_α^a is the active-force density, and $\mathbf{v}^0$ is the flow field corresponding to that uniform-density situation. This flow field, given by Eq. (S17), captured most features of the experimentally measured flow fields around topological defects. However, it did not capture the counterflow measured in front of the $+1/2$ defects (Fig. 4e).

To capture the counterflow, we assume that cells do not readily go into an upper layer in response to non-uniform flows. In this case, pressure gradients build up due to density inhomogeneities in the basal layer. Therefore, the force balance becomes

$$\xi_{\alpha\beta}v_\beta = -\partial_\alpha P + f_\alpha^a, \qquad (S21)$$

where P is the pressure in the basal cell layer. We assume that this pressure depends on the basal cell density through a linear equation of state:

$$P(\rho) = B\frac{\rho - \rho_0}{\rho_0} + P_0, \qquad (S22)$$

where B is the bulk modulus of the monolayer, and $P_0 = P(\rho_0)$ is the pressure of the uniform-density reference state. Introducing Eq. (S22) into Eq. (S21), we obtain

$$\xi_{\alpha\beta}v_\beta = -\frac{B}{\rho_0}\partial_\alpha\rho + f_\alpha^a. \qquad (S23)$$

In principle, not only the pressure but also both the friction coefficient ξ_0 and the active stress coefficient ζ could depend on cell density. Hereafter, in order to show that pressure gradients alone are sufficient to produce a counterflow, we ignore these possible additional dependencies. Moreover, given that the flow field obtained from the uniform-density approximation was close to the experimental measurements, we propose to explain the counterflow based on small perturbations around the uniform-density solution: $\rho(\mathbf{r}) = \rho_0 + \delta\rho(\mathbf{r})$ and $\mathbf{v}(\mathbf{r}) = \mathbf{v}^0(\mathbf{r}) + \delta\mathbf{v}(\mathbf{r})$. For these perturbations, and with the aforementioned assumptions, the force balance Eq. (S23) implies

$$\xi_{\alpha\beta}\delta v_\beta = -\frac{B}{\rho_0}\partial_\alpha\delta\rho. \qquad (S24)$$

To obtain the flows induced by pressure gradients from Eq. (S24), we need to specify the basal cell density field $\rho(\mathbf{r})$. This field obeys the continuity equation

$$\frac{\partial \rho(\mathbf{r},t)}{\partial t} = -\nabla \cdot [\rho(\mathbf{r},t)\mathbf{v}(\mathbf{r},t)] - k_{\text{extr}}(\mathbf{r},t), \qquad \text{(S25)}$$

where $k_{\text{extr}}(\mathbf{r},t)$ is the rate of cell extrusion from the basal monolayer to upper cell layers. If cells readily extrude upon compression, the steady-state extrusion rate is

$$k_{\text{extr}}(\mathbf{r}) = -\nabla \cdot [\rho(\mathbf{r})\mathbf{v}(\mathbf{r})]. \qquad \text{(S26)}$$

In the uniform-density situation of Sections A and B, the extrusion rate reduces to

$$k_{\text{extr}}^0(\mathbf{r}) = -\rho_0 \nabla \cdot \mathbf{v}^0(\mathbf{r}). \qquad \text{(S27)}$$

More generally, when we introduce the small perturbations $\rho(\mathbf{r}) = \rho_0 + \delta\rho(\mathbf{r})$ and $\mathbf{v}(\mathbf{r}) = \mathbf{v}^0(\mathbf{r}) + \delta\mathbf{v}(\mathbf{r})$, Eq. (S26) expands into

$$\begin{aligned}
k_{\text{extr}}(\mathbf{r}) \approx &-\rho_0 \nabla \cdot \mathbf{v}^0(\mathbf{r}) - \rho_0 \nabla \cdot \delta\mathbf{v}(\mathbf{r}) \\
&- \delta\rho(\mathbf{r})\nabla \cdot \mathbf{v}^0(\mathbf{r}) - \mathbf{v}^0(\mathbf{r}) \cdot \nabla\delta\rho(\mathbf{r}). \quad \text{(S28)}
\end{aligned}$$

This expression determines the extrusion rate if cells readily move to a new layer under compression. However, if cells do not readily move to a new layer, the rate of cell extrusion is no longer given by Eq. (S28). Rather, some of the terms on the right-hand side of Eq. (S28) correspond to in-plane density inhomogeneities that do not lead to cell extrusion. Here, we assume that the extrusion rate is given by the first two terms of Eq. (S28), which are proportional to the uniform density ρ_0: $k_{\text{extr}}(\mathbf{r}) = -\rho_0 \nabla \cdot \mathbf{v}(\mathbf{r})$. Consequently, the remaining two terms of Eq. (S28) must balance:

$$\delta\rho(\mathbf{r})\nabla \cdot \mathbf{v}^0(\mathbf{r}) + \mathbf{v}^0(\mathbf{r}) \cdot \nabla\delta\rho(\mathbf{r}) = 0. \qquad \text{(S29)}$$

Equation (S29) is a closed differential equation for the in-plane density perturbation $\delta\rho(\mathbf{r})$. Its solution can then be inserted into Eq. (S24) to obtain the flow perturbations $\delta\mathbf{v}(\mathbf{r})$ that may account for the counterflow.

2. Cell density and velocity perturbations along the defect axis

Here, we obtain an approximate solution of Eq. (S29) along the midline of a $+1/2$ defect. We approximate the divergence of the flow along the midline by its longitudinal component only, i.e. $\nabla \cdot \mathbf{v}^0|_{y=0} \approx \mathrm{d}v_x^0/\mathrm{d}x|_{y=0}$. Moreover, since the flow field along the midline is purely longitudinal, $\mathbf{v}^0(x,0) = v_x^0(x,0)\,\hat{x}$, Eq. (S29) reduces to

$$\delta\rho(x,0)\left.\frac{\mathrm{d}v_x^0}{\mathrm{d}x}\right|_{y=0} + v_x^0(x,0)\left.\frac{\mathrm{d}\delta\rho}{\mathrm{d}x}\right|_{y=0} \approx 0. \qquad \text{(S30)}$$

This equation can be recast as

$$\frac{\mathrm{d}}{\mathrm{d}x}\left(\left.(\delta\rho\, v_x^0)\right|_{y=0}\right) = 0. \qquad \text{(S31)}$$

The solution to this equation is

$$\delta\rho(x,0) = \frac{J}{v_x^0(x,0)}, \qquad \text{(S32)}$$

where J is an undetermined integration constant, which corresponds to a uniform cell flux along the defect midline. Along the midline, the force balance for the velocity perturbation, Eq. (S24), reads

$$\xi_{xx}(x,0)\delta v_x(x,0) = -\frac{B}{\rho_0}\frac{\mathrm{d}\delta\rho(x,0)}{\mathrm{d}x}. \qquad \text{(S33)}$$

Using Eq. (S32), the velocity perturbation can be finally written entirely in terms of the unperturbed velocity field v_x^0 (given in Eq. (S17)):

$$\delta v_x(x,0) = \frac{BJ}{\rho_0\xi_0}\frac{1}{1 - \epsilon S(r)\cos\phi}\frac{1}{(v_x^0(x,0))^2}\frac{\mathrm{d}v_x^0(x,0)}{\mathrm{d}x}. \tag{S34}$$

Along the midline, polar coordinates become $r = |x|$ and $\phi = 0, \pi$ for the positive and negative sides of the $\hat{x}$ axis.

3. Fit to experimental data

Finally, we fit the total velocity profile along the midline,

$$v_x(x,0) = v_x^0(x,0) + \delta v_x(x,0), \qquad \text{(S35)}$$

to the experimental data. Here, $v_x^0(x,0)$ is obtained from Eq. (S17a) and $\delta v_x(x,0)$ is given by Eq. (S34). In addition to the original parameters ℓ, ζ/ξ_0, and ϵ, now there is an additional fitting parameter $\beta \equiv BJ/(\rho_0\xi_0)$ characterizing the compressibility of the cell monolayer and the cell flux due to the associated pressure gradient. The result of the fit is shown in Fig. 4e (yellow curve), and the optimal values of the parameters are listed in Table II. The fact that $\beta < 0$ reflects that $J < 0$, meaning that the cell density increases as the negative $v_x^0(x,0)$ decreases in magnitude when moving away from the defect core (Fig. S5).

Parameter	$+1/2$ defects
ℓ (μm)	3.1 ± 0.1
ζ/ξ_0 (μm^2/min)	2.47 ± 0.09
ϵ	0.63 ± 0.02
β (μm^3/min^2)	-0.32 ± 0.04

Table II: Optimal values of parameters obtained by fitting the velocity profile along the defect midline, taking into account density inhomogeneities due to monolayer compression. The parameter $\beta \equiv BJ/(\rho_0\xi_0)$ is related to the compressibility B of the cell monolayer and to the cell flux $J < 0$ induced by the associated pressure gradient.
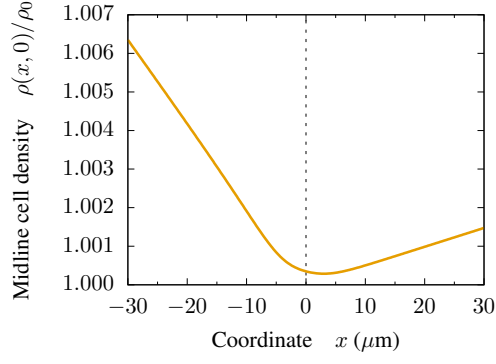
Figure S5: Predicted cell density profile along the midline of
+1/2 defects. The total cell density is $\rho(x, 0) = \rho_0 + \delta\rho(x, 0)$,
where $\delta\rho(x, 0)$ is given by Eq. (S32), with $v_x^0(x, 0)$ obtained from
the fits (parameter values in Table II), and $J = 10^{-4}$ (μm·min)$^{-1}$.